

ARTICLE OPEN



Searching for a route to synthesize in situ epitaxial Pr₂Ir₂O₇ thin films with thermodynamic methods

Lu Guo^{1,4}, Shun-Li Shang^{2,4}, Neil Campbell³, Paul G. Evans¹, Mark Rzchowski³, Zi-Kui Liu² and Chang-Beom Eom¹✉

In situ growth of pyrochlore iridate thin films has been a long-standing challenge due to the low reactivity of Ir at low temperatures and the vaporization of volatile gas species such as IrO₃(g) and IrO₂(g) at high temperatures and high P_{O₂}. To address this challenge, we combine thermodynamic analysis of the Pr-Ir-O₂ system with experimental results from the conventional physical vapor deposition (PVD) technique of co-sputtering. Our results indicate that only high growth temperatures yield films with crystallinity sufficient for utilizing and tailoring the desired topological electronic properties and the in situ synthesis of Pr₂Ir₂O₇ thin films is fettered by the inability to grow with P_{O₂} on the order of 10 Torr at high temperatures, a limitation inherent to the PVD process. Thus, we suggest techniques capable of supplying high partial pressure of key species during deposition, in particular chemical vapor deposition (CVD), as a route to synthesis of Pr₂Ir₂O₇.

npj Computational Materials (2021)7:144; <https://doi.org/10.1038/s41524-021-00610-9>

INTRODUCTION

Complex 5d oxide systems, such as pyrochlore iridates (RE₂Ir₂O₇ with RE = Rare Earth), have an unusual combination of magnetic and structural features that makes them ideal systems for the formation of non-trivial topological phases arising from geometric frustration combined with strong spin-orbit coupling. The spin-orbit-coupled Ir states in RE₂Ir₂O₇ dominate conduction as the Iridium-Oxygen network is much more covalent than the praseodymium-oxygen network^{1–9}. The high entanglement among crystal lattice, strong spin-orbital coupling, and electronic correlation makes the system enticing for thin-film engineering, but this requires high-quality films both in terms of crystallinity and stoichiometry. Synthesis of requisite films has long been impeded due to the volatility of Iridium-Oxygen compounds at temperatures suitable for crystalline growth.

Attempts at in situ growth via physical vapor deposition (PVD) such as magnetron sputtering, pulsed laser deposition (PLD), and molecular beam epitaxy have failed to yield phase-pure epitaxial thin films, leaving most experimental studies limited to bulk systems. In situ synthesis via PVD techniques, such as PLD, shows that this difficulty comes from the low reactivity between Ir and RE oxides combined with the high volatility of the gas phase of Ir oxides such as IrO₃(g)^{10,11}. To overcome this difficulty, solid-phase epitaxy has been successfully used to synthesize RE₂Ir₂O₇ epitaxial thin films^{10,12–15}. This method circumvents the IrO₃(g) volatility dilemma through first depositing amorphous phase at conditions suitable for a stoichiometric balance of elements, then post-annealing at high temperatures in air to induce crystallization. The high temperatures necessary for ex situ crystallization inherently induce surface roughening¹⁶ and intermixing between adjacent heterostructure layers¹⁷, limiting the study of RE₂Ir₂O₇ based on heterostructure design. Advancing the study of electronic properties is thus contingent upon success of in situ synthesis to obtain simultaneous stoichiometric growth with near-perfect crystallinity.

The most common methods for synthesizing high-quality ceramic oxide films all employ PVD. PVD requires that the

constituents of the film be physically moved from a source material to the substrate, upon which they deposit. The substrate temperature and chamber partial pressures are controlled to create thermodynamic conditions for the formation of gas species involved in film deposition when the source materials propagate towards the substrate surface. Governed by thermodynamic properties and growth conditions, the gas species near the substrate surface for deposition can be different from the species in the flux from the source materials¹¹, illustrated in Fig. 1a. Although many materials have been synthesized successfully via the PVD methods, including some iridates with oxygen pressures close to the upper limit for PVD^{18,19}, we show that Pr₂Ir₂O₇ synthesis is thwarted due to the surprising stability of a similar Pr₃IrO₇ phase, as shown in Fig. 1b. Our experimental sampling of the thermodynamic space yielded only the Pr₃IrO₇ phase and other species of the constituents, but not Pr₂Ir₂O₇. Seeking to circumvent the formation of this pernicious Pr₃IrO₇ phase, we calculate the phase diagram for the Pr-Ir-O₂ ternary system using the Calculation of Phase Diagrams (CALPHAD) approach^{20–22} for insight into the thermodynamics of Pr₂Ir₂O₇ synthesis. Our results indicate that the presence of volatile IrO₃(g) is vital to the formation of the desired Pr₂Ir₂O₇ phase and thus indicate that future attempts for in situ growth should be performed under high deposition pressure, utilizing high-pressure sputtering or chemical vapor deposition (CVD).

RESULTS

As the volatilization of the iridium-oxygen compounds, specifically IrO₃, is the prime suspect for Ir deficiency in the synthesis of Pr₂Ir₂O₇, we use computational thermodynamics to predict the vapor pressures of the Ir-O and Pr-O species at conditions relevant to PVD. There are nine relevant gas species in the Pr-Ir-O system based on the Scientific Group Thermodata Europe (SGTE) substance database (SSUB5)²³: Ir, IrO, IrO₂, IrO₃, O, O₂, O₃, PrO, and Pr. The results reveal that IrO₃(g) is the dominant gas species,

¹Department of Materials Science and Engineering, University of Wisconsin-Madison, Madison, Wisconsin, USA. ²Department of Materials Science and Engineering, The Pennsylvania State University, University Park, Pennsylvania, USA. ³Department of Physics, University of Wisconsin-Madison, Madison, Wisconsin, USA. ⁴These authors contributed equally: Lu Guo, Shun-Li Shang. ✉email: eom@engr.wisc.edu

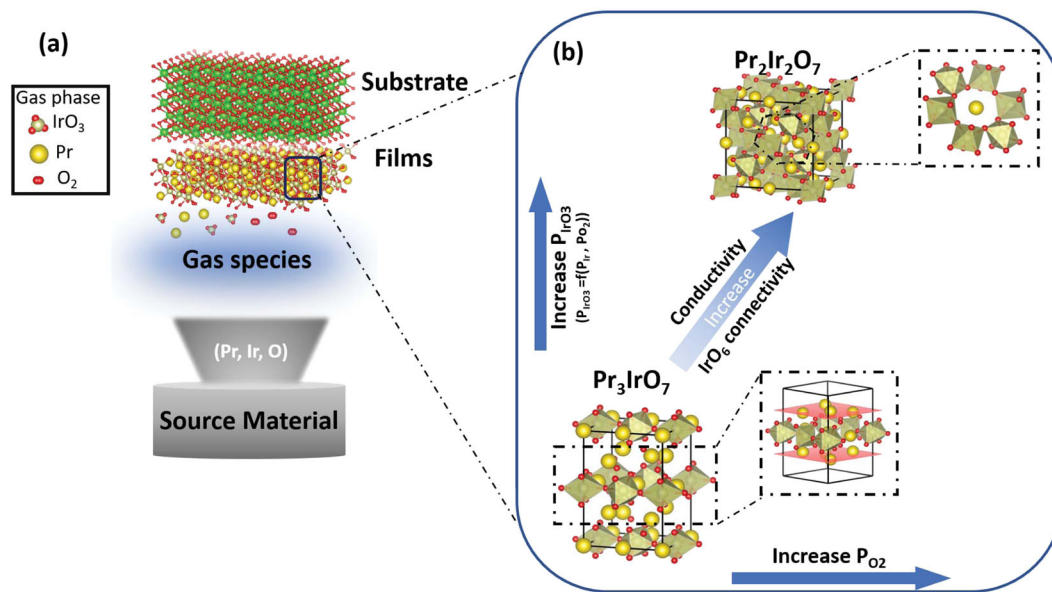


Fig. 1 Schematic in situ co-sputtering thin-film deposition. In the actual experiment, $\text{Pr}_2\text{Ir}_2\text{O}_7$ and IrO_2 targets are simultaneously sputtered, (a). The details are included in Supplementary Fig. 2. The condensation of the vapor species is key to the thin-film synthesis, (b). By synthesizing epitaxial $\text{Pr}_2\text{Ir}_2\text{O}_7$ thin films, we can tailor the properties based on breaking the cubic symmetry. The strong spin-orbital coupling, originating from the Ir, opens paths toward a new generation of spintronics based on frustrated antiferromagnetic (AFM) conductors.

which has a partial pressure up to 1000 times greater than all other gas species in the system, except for molecular oxygen ($\text{O}_2(\text{g})$). We then compute the isothermal phase diagram to elucidate how the relative proportion of supplied constituents from the source materials will impact the compounds that crystallize on the substrate. In the isothermal ternary phase diagram, we identify the Pr_3IrO_7 compound, which is Ir deficient relative to the desired $\text{Pr}_2\text{Ir}_2\text{O}_7$, yet structurally similar. As our primary growth control is via the selection of the gas partial pressures, and almost all iridium in the system oxidizes into $\text{IrO}_3(\text{g})$, we plot potential phase diagrams of partial pressures of gas species $\text{O}_2(\text{g})$ and $\text{IrO}_3(\text{g})$ for various stable compounds from the ternary phase diagram. The relationship between $\text{O}_2(\text{g})$, $\text{IrO}_3(\text{g})$, and the solid-phase compounds serves as a guide to changing growth conditions for $\text{Pr}_2\text{Ir}_2\text{O}_7$ synthesis. The computational calculations are confirmed by thin-film deposition using a range of conditions throughout the relevant thermodynamic windows. Overall, we find that $\text{Pr}_2\text{Ir}_2\text{O}_7$ can only form when both $\text{O}_2(\text{g})$ and $\text{IrO}_3(\text{g})$ partial pressures are high, indicating that $\text{IrO}_3(\text{g})$ appears to be the principal species by which hybridized Ir becomes incorporated into the film crystal. In particular, the $\text{IrO}_3(\text{g})$ partial pressure, the dynamic equilibrium value in the gas phase, must be at or above the equilibrium value at the substrate growth temperature, indicated in Fig. 2, and shown over a wider range in Supplementary Fig. 1. We note that the O : Ir ratio of 3.5 in $\text{Pr}_2\text{Ir}_2\text{O}_7$ is very close to the ratio in $\text{IrO}_3(\text{g})$, and that solid-phase Ir (s) forms in films deposited under conditions of high Ir and low-oxygen partial pressures. These results point to deposition techniques that can support high deposition pressure up to 9 Torr as promising routes toward successful in situ synthesis.

Vapor pressures of the binary systems IrO_2 and Pr_2O_3

As the final film composition is determined by the equilibrium between solid and vapor phases at the substrate temperature, we start by considering the partial pressure vs. temperature relationship for the binary Ir-O and Pr-O systems. As shown in Fig. 2, $\text{IrO}_3(\text{g})$ has the highest partial pressure by at least three orders of magnitude of the species, except Oxygen, throughout the range of temperatures considered. At our growth temperature of 1163 K,

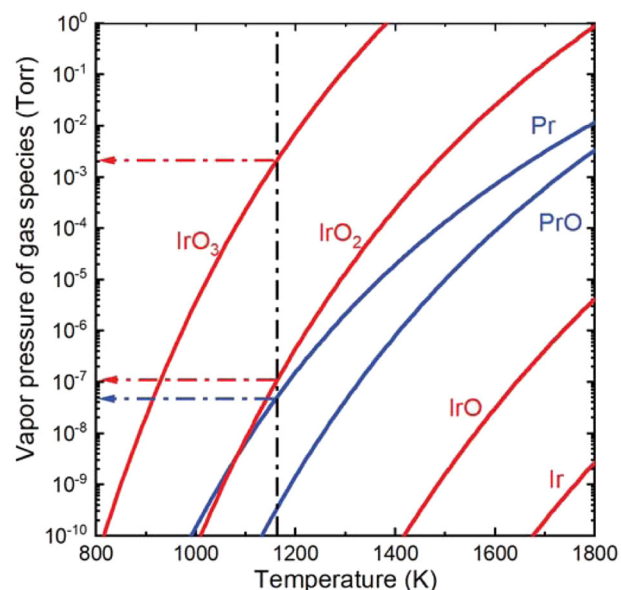


Fig. 2 Partial pressures of gas species in the Ir-O₂ and the Pr-O₂ binary systems. In thermodynamic calculations, the ratios of the components of Ir:O₂ and Pr:O₂ were fixed at 1:1 and 2:1.5, to represent the compositions of IrO₂ and Pr₂O₃, respectively. The vertical dot-dashed black line indicates the growth temperature (1163 K) and the dot-dashed horizontal lines refer to the partial pressure of IrO₃(g), IrO₂(g), and Pr(g) gas species, respectively. More information is shown in Supplementary Fig. 1.

the partial pressure of $\text{IrO}_3(\text{g})$ is 2×10^{-3} Torr. With $\text{O}_2(\text{g})$ in the growth chamber, regardless of the Ir flux type (Ir metal vapor or Ir-O binary compounds, or Ir precursor) provided from the source materials, the dominant Ir flux to the substrate surface is gaseous $\text{IrO}_3(\text{g})$. The partial pressure of $\text{IrO}_3(\text{g})$ depends on the equilibrium of species in gas phase such as $\text{O}_2(\text{g})$ and Ir(g), and is not an independent thermodynamic variable nor an independent experimental growth parameter. This high vapor pressure of $\text{IrO}_3(\text{g})$ explains the common Ir deficiency of thin films²⁴.

By comparison, the most volatile Pr-O species is Pr(g), followed by PrO(g), both of which have partial pressures more than 10^4 times lower than IrO₃(g) at our growth temperature. As such a low partial pressure is easily satisfied by the available O₂(g) and has minimal contribution to total pressure, the Pr-containing compounds condense on the substrate at a much higher rate than the Ir-containing compounds. Our attempt to compensate for this effect, adding a separate IrO₂(s) target as shown in Supplementary Fig. 2, proved insufficient on its own to synthesize in situ Pr₂Ir₂O₇.

Isothermal phase diagram of the Pr-Ir-O₂ system at 1163 K

Having determined the main factors controlling element proportions of gaseous species above the substrate, we utilize a ternary isothermal phase diagram to study which compounds form when

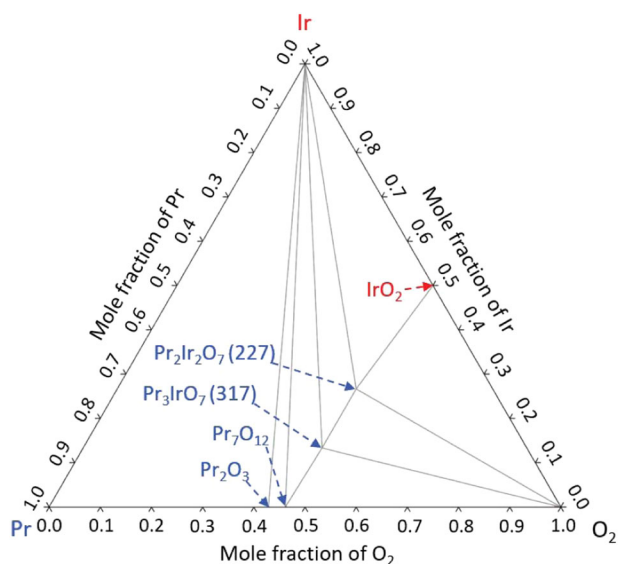


Fig. 3 Calculated isothermal phase diagram of the Pr-Ir-O₂ system with gas phase included. A single point represents the stable condensed phase, the line connecting two points represents the coexistence of the two corresponding phases, and the triangular area connected by three points indicates three-phase invariant equilibria. In the three-phase equilibrium regime around the right bottom corner, the dominant gas species is O₂(g) with other gas species plotted in Supplementary Fig. 1.

different stoichiometries are present on the substrate. We base our calculations on the SSUB5 database²³ for the binary oxides and the formation energies of Pr₂Ir₂O₇ (227) and Pr₃IrO₇ (317) from first-principles calculations, which were further refined by experimental partial pressure of oxygen. The calculated isothermal Pr-Ir-O₂ phase diagram at our deposition temperature of 1163 K and 760 Torr is plotted in Fig. 3 with the stoichiometric phases shown by points, and the two- and three-phase regions shown by lines and areas, respectively. Although the gas phase is dominated by O₂, many other species are present as shown in Fig. 2. We think of the gas phase as necessary to transport constituents to the substrate surface, making the praseodymates important in addition to the higher-partial pressure iridates. First, the calculations do not consider any stable phases along the Ir-Pr binary system axis, because this binary system has not yet been modeled by the CALPHAD method. Possible Ir-Pr phases are not critical for the present work due to the current interest in oxides with much higher stability than the compounds between Ir and Pr under experimental conditions. It can be seen in Fig. 3 that, in addition to the desired Pr₂Ir₂O₇ phase, Pr₃IrO₇ becomes stable at lower Ir concentrations. As a result, we expect that Iridium deficiency will lead to some amount of Pr₃IrO₇ in our films. The Pr₂Ir₂O₇ (227) and Pr₃IrO₇ (317) phases are in equilibrium with the gas phase, forming a three-phase invariant equilibrium region of “317 + 227 + gas.” Figure 3 also shows that Pr₂Ir₂O₇(s) is in equilibrium with the solid Ir(s) and oxides IrO₂(s), whereas Pr₃IrO₇(s) is additionally in equilibrium with Pr₇O₁₂(s). These results indicate that Ir(s) and oxides IrO₂(s), Pr₃IrO₇(s), and Pr₇O₁₂(s) are possible secondary phases during the synthesis of Pr₂Ir₂O₇(s).

Potential phase diagram of the Pr-Ir-O₂ system at 1163 K

Figure 4 illustrates the calculated isothermal Gibbs-potential-derived phase diagram of the Pr-Ir-O₂ system at 1163 K and 760 Torr as a function of the partial pressures of O₂(g) and IrO₃(g)—the two dominant gas species (Fig. 2). The phase diagram shows the species, which minimize the Gibbs thermodynamic potential at each condition. In this potential phase diagram, the cross-points indicate three-phase invariant equilibria, the lines show the two-phase equilibria, and the areas are the single-phase regions. It is understood that when the partial pressure of O₂(g) equals to the total pressure of 760 Torr, the region is a single gas phase. When analyzing the potential phase diagram for growth considerations, we consider the plotted partial pressures as representative of the conditions immediately above the substrate during growth.

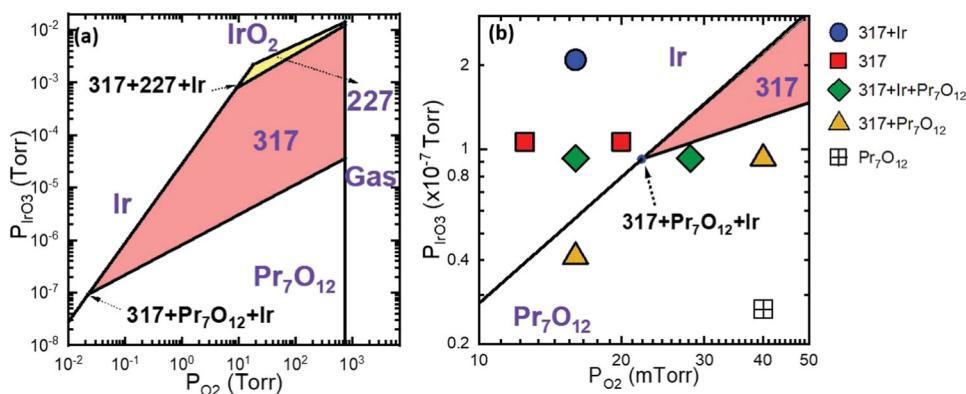


Fig. 4 Calculated potential phase diagram of the Pr-IrO₃-O₂ system. Calculated potential phase diagram of the Pr-IrO₃-O₂ system at 1163 K (890 °C) and total pressure of 1 atm (760 Torr) with the partial pressures of O₂ (P_{O_2}) and IrO₃ (P_{IrO_3}) plotted (a), the zoomed-in diagram and the experimental comparison from the co-sputtering results (b). In the calculated phase diagram, the points represent three-phase equilibrium, the lines two-phase equilibrium, and the areas one-phase equilibrium. Here, 227 represents Pr₂Ir₂O₇ and 317 represents Pr₃IrO₇. The cross-point of “317 + Pr₇O₁₂ + Ir” is located at $[2 \times 10^{-2}, 9 \times 10^{-8}]$ Torr with respect to P_{O_2} and P_{IrO_3} , respectively, whereas the minimum partial pressures are $[9, 8 \times 10^{-4}]$ Torr of the equilibria of “317 + 227 + Ir” in order to form Pr₂Ir₂O₇. It is worth noting that the gas single-phase boundary here located at 760 Torr reflects the 1 atm pressure condition of our calculation.

The most striking aspect of the potential phase diagram is that the compounds with more Ir become stable with lower P_{O_2} for a given P_{IrO_3} , even ones with lower oxygen-to-cation ratios. Although this is apparent for pure-phase Ir(s), it is less so for the sequence of IrO_2 to $Pr_2Ir_2O_7$, to Pr_3IrO_7 at high P_{IrO_3} with increasing P_{O_2} . We attribute this trend to the volatilization of Ir in the presence of $O_2(g)$ as a higher P_{O_2} requires a lower P_{Ir} to maintain the same P_{IrO_3} , stabilizing the phases with lower Ir concentration. At low P_{IrO_3} , P_{O_2} increases with the amount of oxygen towards $Pr_7O_{12}(s)$. Furthermore, pure Ir(s) corresponds to exceedingly large P_{IrO_3} partial pressure at any P_{O_2} within the total pressure constraint. These phase relationships highlight the delicate balance of needing enough oxygen for Ir(s) to hybridize into the film crystal but not too much that it forms a high vapor pressure in equilibrium with the desired phase. Furthermore, as P_{IrO_3} decreases at the same P_{O_2} value, the proportion of Pr present in the solid increases, as seen in the “227” stability adjacent to the IrO_2 region, which has the same Ir oxidation state. When the $O_2(g)$ partial pressure reaches the total pressure of 760 Torr, only the gas phase, dominated by O_2 , is stable, as everything oxidizes to volatile compounds.

Experimentally, we grew thin films via PVD co-sputtering and compared the stabilized phases to the potential phase diagram. We determined which phases we stabilized using X-ray diffraction, as shown in Supplementary Fig. 3. For comparison, the thermodynamic oxygen partial pressure corresponds to the oxygen partial pressure set in the chamber far from the substrate. We consider the Ir flux to be $IrO_3(g)$, because the increase of P_{Ir} proportionally increases P_{IrO_3} under constant P_{O_2} . The number of Ir atoms approximated from the growth rate is plotted in Fig. 4b as the corresponding IrO_3 pressure. By comparing these thin-film growths with thermodynamic calculations (Fig. 4b), it can be seen that the equilibrium-phase dependences on $IrO_3(g)$ and $O_2(g)$ are in agreement. Our experimental observation of the “317 + Pr_7O_{12} + Ir” three-phase invariant equilibrium at higher $IrO_3(g)$ pressure and lower O_2 validates the shape of our CALPHAD results for the Pr-Ir- O_2 system, especially regarding the vital role of oxygen for bonded-Ir incorporation in the resultant thin film.

Due to the pressure limitations inherent in PVD, our experimental films were only able to test the low-pressure portion (≤ 40 mTorr) of the phase diagram. We were unable to synthesize $Pr_2Ir_2O_7$ in situ. We used the “317 + Pr_7O_{12} + Ir” three-phase invariant equilibrium point as a reference to quantitatively compare the current experiments and determined the experimental pressures to be 2×10^{-2} Torr and 9×10^{-8} Torr for P_{O_2} and P_{IrO_3} , respectively. According to this comparison, the minimum P_{O_2} and P_{IrO_3} values needed to stabilize $Pr_2Ir_2O_7$ are 9 Torr and 8×10^{-4} Torr, respectively, which correspond to the “317 + 227 + Ir” three-phase invariant equilibrium. The necessity of high P_{O_2} and P_{IrO_3} partial pressures makes synthesis of this system ideal for growth techniques that can support high-pressure thin-film growth, such as CVD.

Effect of the growth temperature on the phase relationships

We sought to enlarge the $Pr_2Ir_2O_7$ stabilization window by changing the temperature, as, in accordance with Fig. 2, a lower temperature allows for much lower IrO_3 partial pressure. The previously discussed growth temperature of 1163 K was chosen to optimize the kinetic aspects of film growth to ensure single-crystalline films for heterostructure engineering. Thermodynamic calculations, however, indicate that lower growth temperatures could reduce the impact of the requirements for high Ir-component pressures. In addition, thermostability experiments, shown in Supplementary Fig. 4, show $Pr_2Ir_2O_7$ is more stable at 1273 K than at 1373 K. The vapor pressure calculations in Fig. 2 indicate that the equilibrium partial pressure of IrO_3 drops off by orders of magnitude if the growth temperature is lowered to

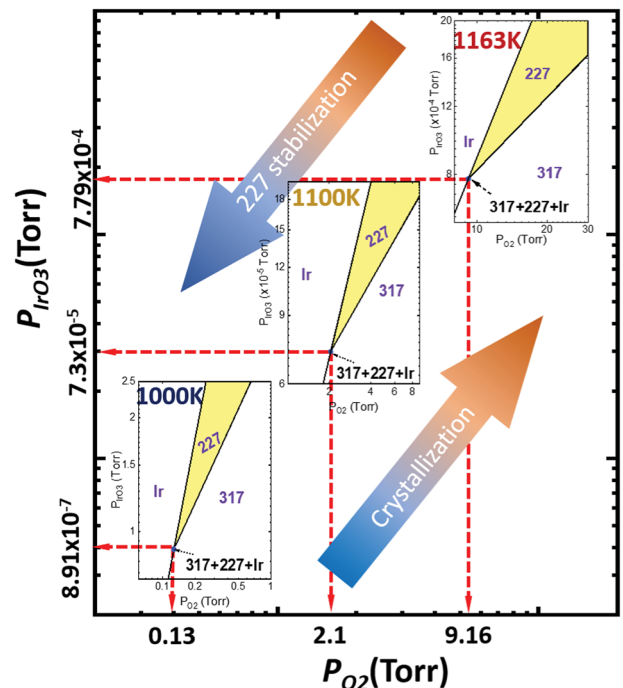


Fig. 5 Calculated potential phase diagrams of the Pr- IrO_3 - O_2 system at 1000, 1100, and 1163 K. In the calculated phase diagrams, the points represent three-phase equilibria, the lines two-phase equilibria, and the areas one-phase equilibria. The dashed red arrows indicate the minimum requirement of IrO_3 and O_2 partial pressures for the 227 phase.

1000 K. Figure 5 illustrates the effects of the temperature on the phase relationships in the Pr-Ir- O_2 system. Calculations at 1000 K indicate that the $Pr_2Ir_2O_7$ phase forms with P_{IrO_3} as low as 9×10^{-7} Torr, which is almost 1000 times lower than that at 1163 K, and that the minimum P_{O_2} value decreased by 70 times from 9.2 Torr at 1163 K to 0.13 Torr at 1000 K. The same relationship between P_{IrO_3} and P_{O_2} to maintain $Pr_2Ir_2O_7$ phase stability occurs at 1000 K; notably, the interplay of increasing P_{IrO_3} coinciding with increasing P_{O_2} . These results also indicate that phase stability at fixed partial pressures is very sensitive to temperature, resulting in a narrow growth window for $Pr_2Ir_2O_7$.

Unfortunately, our experimental films grown below 1073 K showed poor crystallinity, negating the benefits of the $Pr_2Ir_2O_7$ phase for heterostructuring applications that demand high-quality films, forcing us to pursue high-pressure in situ growth such as CVD in the future.

DISCUSSION

In summary, we utilized the CALPHAD modeling technique to explore thermodynamic properties of the Pr-Ir- O_2 system and find that $Pr_2Ir_2O_7$ can only form high-quality crystals above 1073 K and under oxygen partial pressures much higher ($P_{O_2} > 9$ Torr). These conditions cannot be achieved with conventional PVD methods and provide insights into why PVD is an inadequate synthesis pathway. However, these conditions can be accessed in CVD growth. Our study, therefore, suggests exploring CVD growth for high-quality $Pr_2Ir_2O_7$ films.

METHODS

Details of thermodynamic calculations

Thermodynamic calculations of the Pr-Ir- O_2 system were performed by the Thermo-Calc software²⁵ in terms of the SSUB5 database²³. Structural space groups from the Materials project, used for phonon calculations, are shown

in Supplementary Table 1. The thermodynamic properties of ternary compounds of interest, i.e., $\text{Pr}_2\text{Ir}_2\text{O}_7$ and Pr_3IrO_7 , absent in the SSUB5 database, can be estimated with respect to binary oxides as follows,



In the present work, the reaction entropies for Eqs. (1) and (2) are assumed to be zero, because there is no net change of gas species involved²⁶. The reaction Gibbs energies, $\Delta G_{\text{reaction}}$, contain only the reaction enthalpies and are determined by the following two experimental data: (i) the partial pressure of O_2 , $P_{\text{O}_2} = 22 \pm 6$ mTorr (16 and 28 mTorr, see Fig. 4b), for the invariant equilibrium of “ $\text{Pr}_3\text{IrO}_7 + \text{Ir} + \text{Pr}_2\text{O}_3$ ” at 1163 K and (ii) the $\text{Pr}_2\text{Ir}_2\text{O}_7$ (227) phase decomposes at around 1400 K. The details are described in the Supplementary Information. It is noteworthy that the decomposition temperature of Pr_3IrO_7 is unknown. The Gibbs free energy differences $\Delta G_{\text{reaction}} = -8.72 \text{ kJ mol}^{-1} \text{ atom}^{-1}$ for $\text{Pr}_2\text{Ir}_2\text{O}_7$ (see Eq. (1)) and $\Delta G_{\text{reaction}} = -13.30 \text{ kJ mol}^{-1} \text{ atom}^{-1}$ for Pr_3IrO_7 (see Eq. (2)) were obtained in the present work. These two $\Delta G_{\text{reaction}}$ values are lower than those from the density functional theory (DFT) based first-principles calculations; see details in Supplementary Table 2 and Supplementary Methods in the Supplementary Information. However, these $\Delta G_{\text{reaction}}$ values from experiments agree with the observation that the DFT-based results of enthalpy of formation are in general higher than experimental data by, e.g., 10–40%²⁷; see the comparisons in Supplementary Table 2 in the Supplementary Information.

The influence of interfacial energy and strain energy on the phase diagram were not included in the calculation^{28,29}. These contributions, which are widely used to tailor the growth of thin films, are controlled mainly by the gas phase under deposition conditions. For bulk films, interfacial energy and strain energy play limited roles. The strain energy can expand some phase regions and shrink other phase regions. In most cases of epitaxial thin films, the substrate is chosen to favor the phase of interest, thus expanding its stability window. The growth windows from our thermodynamic calculations thus work well in most cases. Thermodynamic predictions of the regime for stable phase formation has been demonstrated for a number of cases such as the in situ epitaxial thin films of MgB_2 ^{30,31} and Sr_3SnO_3 ³², and the adsorption-controlled epitaxial thin films of SrRuO_3 and CaRuO_3 ³³, La-doped BaSnO_3 ³⁴, PbTiO_3 ³⁵, LuFe_2O_4 ³⁶, BiMnO_3 ³⁷, and BiFeO_3 ³⁸. In addition, the calculations of phase diagrams and potential diagrams (Figs. 2–5) in the present work were performed using Thermo-Calc²⁵; see more details in our previous work¹¹.

Experimental details of co-sputtering

We used co-sputtering for the experimental study of phase formation in the Pr-Ir-O₂ system, a conventional PVD method. In our co-sputtering deposition system (detailed geometry included in the Supplementary Information), the flux of $\text{Pr}_2\text{Ir}_2\text{O}_7$ and IrO_2 can be controlled separately by the voltage applied to each radiofrequency magnetron sputtering gun. The simultaneous sputtering from both $\text{Pr}_2\text{Ir}_2\text{O}_7$ and IrO_2 targets gives the extra tunability of partial pressures of Iridium and its gaseous species. The controllability of these parameters guarantees a direct comparison of the conditions between experiments and thermodynamic predictions.

DATA AVAILABILITY

The data that support the findings of the work are in the manuscript's main text and Supplementary Information. Additional data are available from the corresponding author upon reasonable request.

CODE AVAILABILITY

The commercial codes, Thermo-Calc (www.thermocalc.com) and VASP (www.vasp.at), were used in the present work.

Received: 19 September 2020; Accepted: 11 August 2021;

Published online: 09 September 2021

REFERENCES

1. Matsuhira, K., Wakeshima, M., Hinatsu, Y. & Takagi, S. Metal–insulator transitions in pyrochlore oxides $\text{Ln}_2\text{Ir}_2\text{O}_7$. *J. Phys. Soc. Jpn* **80**, 094701 (2011).

- Nakayama, M. et al. Slater to Mott crossover in the metal to insulator transition of $\text{Nd}_2\text{Ir}_2\text{O}_7$. *Phys. Rev. Lett.* **117**, 056403 (2016).
- Ueda, K. et al. Variation of charge dynamics in the course of metal–insulator transition for pyrochlore-type $\text{Nd}_2\text{Ir}_2\text{O}_7$. *Phys. Rev. Lett.* **109**, 136402 (2012).
- Nakatsui, S. et al. Metallic spin-liquid behavior of the geometrically frustrated Kondo lattice $\text{Pr}_2\text{Ir}_2\text{O}_7$. *Phys. Rev. Lett.* **96**, 087204 (2006).
- Tomiyasu, K. et al. Emergence of magnetic long-range order in frustrated pyrochlore $\text{Nd}_2\text{Ir}_2\text{O}_7$ with metal–insulator transition. *J. Phys. Soc. Jpn* **81**, 034709 (2012).
- Shapiro, M. C. et al. Structure and magnetic properties of the pyrochlore iridate $\text{Y}_2\text{Ir}_2\text{O}_7$. *Phys. Rev. B* **85**, 214434 (2012).
- Disseler, S. M. et al. Magnetic order in the pyrochlore iridates $\text{A}_2\text{Ir}_2\text{O}_7$ (A = Y, Yb). *Phys. Rev. B* **86**, 14428 (2012).
- Donnerer, C. et al. All-in–all-out magnetic order and propagating spin waves in $\text{Sm}_2\text{Ir}_2\text{O}_7$. *Phys. Rev. Lett.* **117**, 037201 (2016).
- Sagayama, H. et al. Determination of long-range all-in–all-out ordering of Ir4+ moments in a pyrochlore iridate $\text{Eu}_2\text{Ir}_2\text{O}_7$ by resonant x-ray diffraction. *Phys. Rev. B Condens. Matter Mater. Phys.* **87**, 100403 (2013).
- Fujita, T. C. et al. Odd-parity magnetoresistance in pyrochlore iridate thin films with broken time-reversal symmetry. *Sci. Rep.* **5**, 9711 (2015).
- Adkison, K. M. K. M. et al. Suitability of binary oxides for molecular-beam epitaxy source materials: a comprehensive thermodynamic analysis. *APL Mater.* **8**, 081110 (2020).
- Gallagher, J. C. et al. Epitaxial growth of iridate pyrochlore $\text{Nd}_2\text{Ir}_2\text{O}_7$ films. *Sci. Rep.* **6**, 22282 (2016).
- Ohtsuki, T. et al. Strain-induced spontaneous Hall effect in an epitaxial thin film of a Luttinger semimetal. *Proc. Natl Acad. Sci. USA* **116**, 8803–8808 (2019).
- Ohtsuki, T., Tian, Z., Halim, M., Nakatsui, S. & Lippmaa, M. Growth of $\text{Pr}_2\text{Ir}_2\text{O}_7$ thin films using solid phase epitaxy. *J. Appl. Phys.* **127**, 035303 (2020).
- Guo, L. et al. Spontaneous Hall effect enhanced by local Ir moments in epitaxial $\text{Pr}_2\text{Ir}_2\text{O}_7$ thin films. *Phys. Rev. B* **101**, 104405 (2020).
- Gao, H. & Nix, W. D. Surface roughening of heteroepitaxial thin films. *Annu. Rev. Mater. Sci.* **29**, 173–209 (1999).
- Hulko, O., Thompson, D. A. & Simmons, J. G. Semiconductor science and technology quantitative compositional profiles of enhanced intermixing in GaAs/AlGaAs quantum well heterostructures annealed with and without a SiO_2 cap layer. *Semicond. Sci. Technol.* **24**, 045015 (2009).
- Anderson, T. J. et al. Metastable honeycomb $\text{SrTiO}_3/\text{SrIrO}_3$ heterostructures. *Appl. Phys. Lett.* **108**, 151604 (2016).
- Anderson, T. J. et al. Interfacial B-site atomic configuration in polar (111) and non-polar (001) $\text{SrIrO}_3/\text{SrTiO}_3$ heterostructures. *APL Mater.* **5**, 096110 (2017).
- Liu, Z. K. First-principles calculations and CALPHAD modeling of thermodynamics. *J. Phase Equilibria Diffus.* **30**, 517–534 (2009).
- Saunders, N. & Miodownik, A. P. *CALPHAD (Calculation of Phase Diagrams): A Comprehensive Guide* (Pergamon, 1998).
- Liu, Z. K. Computational thermodynamics and its applications. *Acta Mater.* **200**, 745–792 (2020).
- Scientific Group Thermodata Europe (SGTE), *Thermodynamic Properties of Inorganic Materials. Landolt-Boernstein New Series, Group IV.* Vol. 19 (Springer, 1999).
- Kim, W. J., Ko, E. K., Kim, S. Y., Kim, B. & Noh, T. W. In-operando spectroscopic ellipsometry studies of IrO_2 dynamic instabilities: guide to in-situ growth of pyrochlore iridate thin films. *Curr. Appl. Phys.* **19**, 400–405 (2019).
- Andersson, J. O. et al. Thermo-Calc & Dictra, computational tools for materials science. *Calphad* **26**, 273–312 (2002).
- Liu, Z. K. & Wang, Y. *Computational Thermodynamics of Materials* (Cambridge Univ. Press, 2016).
- Shang, S.-L., Wang, Y., Anderson, T. J. & Liu, Z.-K. Achieving accurate energetics beyond (semi-)local density functional theory: illustrated with transition metal disulfides, $\text{Cu}_2\text{ZnSnS}_4$, and Na_3PS_4 related semiconductors. *Phys. Rev. Mater.* **3**, 015401 (2019).
- Shen, J. Y., Johnston, S., Shang, S. L. & Anderson, T. Calculated strain energy of hexagonal epitaxial thin films. *J. Cryst. Growth* **240**, 6–13 (2002).
- Shang, S.-L. et al. Lateral versus vertical growth of two-dimensional layered transition-metal dichalcogenides: thermodynamic insight into MoS_2 . *Nano Lett.* **16**, 5742–5750 (2016).
- Liu, Z. K., Schlom, D. G., Li, Q. & Xi, X. X. Thermodynamics of the Mg–B system: implications for the deposition of MgB_2 thin films. *Appl. Phys. Lett.* **78**, 3678 (2001).
- Zeng, X. H. et al. In situ epitaxial MgB_2 thin films for superconducting electronics. *Nat. Mater.* **1**, 35–38 (2002).
- Ma, Y. et al. Realization of epitaxial thin films of the topological crystalline insulator Sr_3SnO . *Adv. Mater.* **32**, 2000809 (2020).
- Nair, H. P. et al. Synthesis science of SrRuO_3 and CaRuO_3 epitaxial films with high residual resistivity ratios. *APL Mater.* **6**, 046101 (2018).

34. Paik, H. et al. Adsorption-controlled growth of La-doped BaSnO₃ by molecular-beam epitaxy. *APL Mater.* **5**, 116107 (2017).
35. Smith, E. H. et al. Exploiting kinetics and thermodynamics to grow phase-pure complex oxides by molecular-beam epitaxy under continuous codeposition. *Phys. Rev. Mater.* **1**, 023403 (2017).
36. Brooks, C. M. et al. The adsorption-controlled growth of LuFe₂O₄ by molecular-beam epitaxy. *Appl. Phys. Lett.* **101**, 132907 (2012).
37. Lee, J. H. et al. Adsorption-controlled growth of BiMnO₃ films by molecular-beam epitaxy. *Appl. Phys. Lett.* **96**, 262905 (2010).
38. Ihlefeld, J. F. et al. Adsorption-controlled growth of BiFeO₃ by MBE and integration with wide band. *IEEE Trans. Ultrason. Ferroelectr. Frequency Control* **56**, 1528–1533 (2009).

ACKNOWLEDGEMENTS

Synthesis of thin films at the University of Wisconsin-Madison was supported by NSF through the University of Wisconsin Materials Research Science and Engineering Center (DMR-1720415), the Gordon and Betty Moore Foundation's EPIQS Initiative, grant GBMF9065 to C.B.E., and Vannevar Bush Faculty Fellowship (N00014-20-1-2844). Thin-film characterizations at the University of Wisconsin-Madison was supported by the US Department of Energy (DOE), Office of Science, Office of Basic Energy Sciences, under award number DEFG02-06ER46327. S.L.S. and Z.K.L. acknowledge partial financial support from the National Science Foundation (NSF) through Grant number CMMI-1825538 and the Dorothy Pate Enright Professorship. First-principles calculations were carried out partially on the ACI clusters at the Pennsylvania State University, partially on the resources of the National Energy Research Scientific Computing Center (NERSC) supported by the U.S. Department of Energy Office of Science User Facility operated under Contract number DE-AC02-05CH11231, and partially on the resources of the Extreme Science and Engineering Discovery Environment (XSEDE) supported by National Science Foundation with Grant number ACI-1548562. We thank T. Nan, A. Edgeton, J.W. Lee, and Y. Yao for helpful discussion.

AUTHOR CONTRIBUTIONS

L.G. and C.B.E. conceived the project. C.B.E., M.S.R., and P.G.E. supervised experimental work and Z.K.L. supervised thermodynamic calculations. L.G. performed the films

growth and structural characterizations. S.L.S. performed thermodynamic calculations. L.G., N.G.C., and S.L.S. wrote the manuscript. C.B.E. directed the research.

COMPETING INTERESTS

The authors declare no competing interests.

ADDITIONAL INFORMATION

Supplementary information The online version contains supplementary material available at <https://doi.org/10.1038/s41524-021-00610-9>.

Correspondence and requests for materials should be addressed to Chang-Beom Eom

Reprints and permission information is available at <http://www.nature.com/reprints>

Publisher's note Springer Nature remains neutral with regard to jurisdictional claims in published maps and institutional affiliations.



Open Access This article is licensed under a Creative Commons Attribution 4.0 International License, which permits use, sharing, adaptation, distribution and reproduction in any medium or format, as long as you give appropriate credit to the original author(s) and the source, provide a link to the Creative Commons license, and indicate if changes were made. The images or other third party material in this article are included in the article's Creative Commons license, unless indicated otherwise in a credit line to the material. If material is not included in the article's Creative Commons license and your intended use is not permitted by statutory regulation or exceeds the permitted use, you will need to obtain permission directly from the copyright holder. To view a copy of this license, visit <http://creativecommons.org/licenses/by/4.0/>.

© The Author(s) 2021